Phil. Trans. R. Soc. A.
DOI: https://doi.org/10.1098/rsta.2020.0397

A unified lattice Boltzmann model and application to multiphase flows

Kai H. Luo[1]*, Linlin Fei[2], Geng Wang[1]

1 Department of Mechanical Engineering, University College London, Torrington Place, London WC1E 7JE, UK
2 Chair of Building Physics, Department of Mechanical and Process Engineering, ETH Zürich (Swiss Federal Institute of Technology in Zürich), Zürich 8092, Switzerland

Keywords: Lattice Boltzmann model, mesoscale modelling, multiphase flow, thermal flow, phase change

Abstract

In this work, we develop a unified lattice Boltzmann model (ULBM) framework that can seamlessly integrate the widely used lattice Boltzmann collision operators, including the Bhatnagar-Gross-Krook (BGK) or single-relation-time (SRT), multiple-relaxation-time (MRT), central-moment or cascaded lattice Boltzmann method (CLBM), and multiple entropic operators (KBC). Such a framework clarifies the relations among the existing models and greatly facilitates model comparison and development as well as coding. Importantly, any LB model or treatment constructed for a specific collision operator could be easily adopted by other operators. We demonstrate the flexibility and power of the ULBM framework through three multiphase flow problems: the rheology of an emulsion, splashing of a droplet on a liquid film, and dynamics of pool boiling. Further exploration of ULBM for a wide variety of phenomena would be both realistic and beneficial, making the lattice Boltzmann method (LBM) more accessible to non-specialists.

1. Introduction

The lattice Boltzmann method (LBM), derived from the general kinetic theory, has achieved remarkable success for numerical simulations of complex fluid flows and beyond [1–4]. The LBM solves the discrete Boltzmann equation for distribution functions, using a highly efficient collision-streaming two-step algorithm. The basic LBM formulation is designed to reproduce the incompressible Navier-Stokes (N-S) equations in the low-Mach limit, and more advanced models have been developed for compressible, multiphase, reactive, multiphysics flows [3–5]. As an emergent simulation method, a huge number of models and numerical treatments have been developed over the past three decades, without a unified formulation.

In terms of the LB collision operator, the Bhatnagar-Gross-Krook (BGK) or single-relaxation-time (SRT) model, in which all the distributiion functions relax to their local equilibria at an identical rate [6], is the simplest. However, the simplicity of the SRT operator comes at the expense of numerical instability with increasing Reynolds number and inaccuracy in dealing with non-slip boundary conditions [7,8]. An improved model is the multiple relaxation time (MRT) operator, whereby the distribution functions are first transformed to the raw moments and the collision step is executed in the moment space. Individual relaxation times could be used for different moments or kinetic modes in MRT, leading to improved stability and more freedom to

*Author for correspondence (K.Luo@ucl.ac.uk).
Department of Mechanical Engineering, University College London,
Torrington Place, London WC1E 7JE, UK

achieve non-slip boundary conditions [8,9], though MRT may be associated with reduced accuracy for capturing interfacial dynamics [10]. The cascaded (or central-moment-based) lattice Boltzmann method (CLBM) employs central moments in a co-moving frame in contrast to the raw moments in the stationary frame used in MRT, which improves the numerical stability further [11,12]. In the so-called KBC model, entropic considerations are employed to alter the relaxation parameter for high-order central moments by splitting the contribution to each distribution function into the kinematic part, shear part, and high-order part [13,14]. Each more sophisticated operator offers some improved performance while the computational complexity is also enhanced. To reduce the computational cost, non-orthogonal rather than classical orthogonal basis vectors can be chosen in the moments-based (raw or central) collision operators [15–17]. However, the different relaxation operators/models have been proposed and developed separately and the relations among them have not been systematically clarified so far. As each operator has been employed in conjunction with different physical models for different types of physical problems, it is not always clear how to select the best combination of a collision operator and physical models for a specific physical problem.

Multiphase flows are ubiquitous in nature, biological systems and engineering applications, which typically involve nonlinear, nonequilibrium and multiscale phenomena. Their complexity and diversity are reflected in the large number of physical parameters that influence the multiphase flow behaviours over a wide range of conditions. The LBM has proven to be advantageous in simulating multiphase flows thanks to its mesoscopic nature derived from the kinetic theory [1–4]. Four main types of approaches have emerged since the 1990s: the color-gradient [18,19], phase-field [20,21], free-energy [22,23], and pseudopotential LBMs [24,25]. In particular, the pseudo-potential LBM allows (1) equation of state for non-ideal fluids; (2) non-zero surface tension; (3) natural phase transition; (4) interface formation, deformation, merging, and breakup. Moreover, all the above features are achieved at a minimum programming effort [12]. On the other hand, the original pseudopotential LBM [24,25] suffers from thermodynamic inconsistency, limited parameter ranges (e.g. liquid-to-gas density ratio < 10), density-ratio-dependent surface tension and large spurious currents. Much work has been conducted over the last two decades to overcome these limitations. Significant progress has been made in the following areas: (a) dramatically reduced spurious currents [10,24,25]; (b) high density ratio [10,26–28]; (c) density-independent surface tension implementation [32,33]; (d) contact angle treatment [34,35]; and so on. These have been achieved through enhanced thermodynamic consistency, conformation to Galilean invariants, and consequently, improved forcing schemes [4]. It is clear that a large number of models and methods have been developed for multiphase flow, which can serve as an ideal testbed for developing a unified modelling framework.

In this work, we integrate all the above collision models into a unified lattice Boltzmann model (ULBM) framework and test it in benchmark cases of multiphase flows. We show that various advances in the LB models for multiphase flows can be straightforwardly incorporated into the present framework to enable simulation of complex multiphase problems with realistic parameters. The resulting ULBM framework brings several significant advantages: 1) the relations among different collision operators are clarified, 2) switching between different models within one computer code is straightforward to facilitate model comparison and selection, and 3) any improved model constructed for one collision operator can be easily adopted by other operators. As a result, strengths in different LB models can be integrated to create more powerful models, and new models can be rapidly exploited by different LB formulations and codes. The rest of the paper is organized as follows: Section II gives a detailed description of the ULBM framework. Section III showcases the power of ULBM through multiphase/thermal flow simulations. Finally, discussions and conclusions are provided in Sec. IV.

2. Model description

The LBM solves a discrete Boltzmann equation for the distribution function $f_i(\boldsymbol{x},t)$, designed to recover the macroscopic conservation laws in the macroscopic limit. The distribution function, $f_i(\boldsymbol{x},t) \equiv f(\boldsymbol{x},\boldsymbol{v}=\boldsymbol{e}_i,t)$,

denotes the probability of finding a particle at the spatial point $\boldsymbol{x}$ and time t, with molecular velocity $\boldsymbol{v} = \boldsymbol{e}_i$ [26]. The fluid particles reside in a regular lattice, collide locally and then stream from one lattice node to another along with the discrete velocity $\boldsymbol{e}_i$. This enables a simple and highly efficient "collision-streaming" LBM algorithm, and the streaming step is independent of the collision step:

$$f_i(\boldsymbol{x}+\Delta\boldsymbol{x}, t+\Delta t) = f_i^*(\boldsymbol{x}, t), \tag{1}$$

where $\Delta\boldsymbol{x} = \boldsymbol{e}_i \Delta t$ and Δt are the lattice space and time steps, respectively. For ease of discussion, we first consider the D2Q9 lattice [6], and the discrete velocities $\mathbf{e}_i = \left[\left|e_{ix}\right\rangle, \left|e_{iy}\right\rangle\right]$ are defined as,

$$\begin{aligned} \left|e_{ix}\right\rangle &= [0,1,0,-1,0,1,-1,-1,1]^\top, \\ \left|e_{iy}\right\rangle &= [0,0,1,0,-1,1,1,-1,-1]^\top. \end{aligned} \tag{2}$$

where $i = 0...8$, $\left|\cdot\right\rangle$ denotes a nine-dimensional column vector, and the superscript $\top$ is the transposition symbol.

The key is the post-collision distribution function, f_i^*, which differs according to the collision model constructed. In this work, we show that all the afore-mentioned collision operators can be integrated into a framework of a unified lattice Boltzmann model (ULBM). To construct the ULBM framework, we first define the raw and central moments of f_i^*,

$$k_{mn} = \left\langle f_i \left| e_{ix}^m e_{iy}^n \right\rangle, \qquad \tilde{k}_{mn} = \left\langle f_i \left| (e_{ix}-u_x)^m (e_{iy}-u_y)^n \right\rangle \right. \tag{3}$$

where u_x and u_y are the velocity components in x and y directions, respectively. In the ULBM framework, the post-collision distribution function is expressed as:

$$f_i^*(\mathbf{x}, t) = f_i(\mathbf{x}, t) - (\mathbf{M}^{-1}\mathbf{N}^{-1}\mathbf{S}\mathbf{N}\mathbf{M})\left[f_i(\mathbf{x}, t) - f_i^{eq}(\mathbf{x}, t) \right] \tag{4}$$

where the transformation matrix $\mathbf{M}$ is used to transform the distribution function to its raw moments, k_{mn}^{eq} and $\tilde{k}_{mn}^{eq}$ are defined accordingly by replacing f_i with the discrete equilibrium distribution function f_i^{eq} in the above. The shift matrix $\mathbf{N}$ converts the raw moments (in MRT) of the distribution function into central moments (in CLBM), and the relaxation matrix $\mathbf{S}$ contains the relaxation rates for different moments.

By default, the ULBM provides a concise implementation of CLBM. To this aim, a set of central moments need to be specified. As discussed in [11,15,36,37], the zero-order moment $\tilde{k}_{00}$ (density) and first-order moments $\tilde{k}_{10}$ and $\tilde{k}_{01}$ (momentum components) should be included due to mass and momentum conservations. The second-order moments, $\tilde{k}_{20} + \tilde{k}_{02}$ (trace of the pressure tensor), $\tilde{k}_{20} - \tilde{k}_{02}$ (the normal stress difference), and $\tilde{k}_{11}$ (the off-diagonal component of the pressure tensor) are chosen such that the model allows correct representation of the kinematic and bulk viscosity terms in the hydrodynamic equations. With the high order linearly independent moments, the central moment set is given as:

$$\left|\tilde{T}_i\right\rangle = \mathbf{N}\left|T_i\right\rangle = \mathbf{N}\mathbf{M}\left|f_i\right\rangle = \left[\tilde{k}_{00}, \tilde{k}_{10}, \tilde{k}_{01}, \tilde{k}_{20}+\tilde{k}_{02}, \tilde{k}_{20}-\tilde{k}_{02}, \tilde{k}_{11}, \tilde{k}_{21}, \tilde{k}_{12}, \tilde{k}_{22}\right]^\top \tag{5}$$

where $\left|T_i\right\rangle$ is the corresponding raw moment set,

$$\left|T_i\right\rangle = \left[k_{00}, k_{10}, k_{01}, k_{20}+k_{02}, k_{20}-k_{02}, k_{11}, k_{21}, k_{12}, k_{22}\right]^\top \tag{6}$$

The explicit formulation of $\mathbf{N}$ can be obtained according to the binomial expansion of each central moment by raw moments of that order and below. Therefore, the shift matrix $\mathbf{N}$ is a lower triangular matrix. Due to the symmetry, its inverse matrix $\mathbf{N}^{-1}$ is also lower triangular, with the only difference from $\mathbf{N}$ in that all the odd order velocity terms have opposite signs [17,38]. As discussed in [11,15,17,36,38], the equilibrium central

moments $\left|\tilde{T}_i^{eq}\right\rangle$ are defined as the continuous central moments of the Maxwell-Boltzmann distribution in the continuous velocity space, namely

$$\left|\tilde{T}_i^{eq}\right\rangle = \left[\rho, 0, 0, 2\rho c_s^2, 0, 0, 0, 0, \rho c_s^4\right]^\top \tag{7}$$

where ρ is the fluid density and $c_s = 1/\sqrt{3}$ is the lattice sound speed. In such a case, f_i^{eq} is a "general" local distribution. According to the relation $\mathbf{NM}\left|f_i^{eq}\right\rangle$, it could be verified that the local distribution is a fourth-order Hermite expansion of the Maxwell-Boltzmann distribution [39].

Within the ULBM formulation, when **N = I**, a unity matrix, the ULBM degrades into an MRT operator,

$$f_i^*(\mathbf{x},t) = f_i(\mathbf{x},t) - (\mathbf{M}^{-1}\mathbf{S}\mathbf{M})\left[f_i(\mathbf{x},t) - f_i^{eq}(\mathbf{x},t)\right] \tag{8}$$

Remarkably, such an MRT is slightly different from the classical MRT model expressed by Lallemandal and Luo [8], where the raw moment set is chosen based on the orthogonal constraint of the moment basis vectors. Therefore, the transformation matrix $\mathbf{M}$ of Lallemandal and Luo is orthogonal while the present $\mathbf{M}$ is non-orthogonal and more concise. Thanks to such a choice, the resulting non-orthogonal MRT model retains the numerical accuracy and stability while reducing the computational cost compared with the classical orthogonal MRT model [15,40], especially for three-dimensional simulations [41,42]. For both CLBM and non-orthogonal MRT model, the relaxation matrix $\mathbf{S}$ is diagonal, $\mathbf{S} = diag(1,1,1,s_{2b},s_2,s_2,s_3,s_3,s_4)$, where s_2 and s_{2b} are related to the kinematic viscosity, $\nu = (1/s_2 - 0.5)c_s^2\Delta t$ and bulk viscosity, $\nu_b = (1/s_{2b} - 0.5)c_s^2\Delta t$, respectively. The high-order relaxation rates can be tuned to improve the numerical stability or enforce the nonslip wall boundary condition.

Further, if $\mathbf{S} = (1/\tau)\mathbf{I}$, then the ULBM reduces to the classical SRT scheme [6],

$$f_i^*(\mathbf{x},t) = f_i(\mathbf{x},t) - \frac{1}{\tau}\left[f_i(\mathbf{x},t) - f_i^{eq}(\mathbf{x},t)\right] \tag{9}$$

with a fourth-order-Hermite-expansion f_i^{eq} and $\tau = 1/s_2 = \nu/(c_s^2\Delta t) + 0.5$.

In this way, SRT, MRT, and CLBM schemes are unified [38]. The present ULBM formulation could be further enriched through the incorporation of the entropic stabilizing condition [10,38]:

$$\mathbf{S} = diag(1,1,1,s_2,s_2,s_2,\gamma s_2,\gamma s_2,\gamma s_2) \tag{10}$$

where γ is the entropic stabilizer,

$$\gamma = \frac{1}{s_2} - (1-\frac{1}{s_2})\sum_i \frac{\Delta s_i \Delta h_i}{f_i^{eq}} \Big/ \sum_i \frac{\Delta h_i \Delta h_i}{f_i^{eq}} \tag{11}$$

where $\Delta s_i = s_i - s_i^{eq}$ and $\Delta h_i = h_i - h_i^{eq}$ represent the deviations from the equilibria for the shear part and high-order part of the distribution function. Usually, the shear part means the second-order moments (k_{20}, k_{02}, k_{11}), which could be explicitly obtained by:

$$s_i = \mathbf{M}^{-1}\mathbf{N}^{-1}\left|\tilde{T}_s\right\rangle \tag{12}$$

where the shear part vector $\left|\tilde{T}_s\right\rangle$ is:

$$\left|\tilde{T}_s\right\rangle = \left[0,0,0,\tilde{k}_{20}+\tilde{k}_{02},\tilde{k}_{20}-\tilde{k}_{02},\tilde{k}_{11},0,0,0\right]^\top \tag{13}$$

Similarly, the high-order part of the distribution function can be calculated by $h_i = \mathbf{M}^{-1}\mathbf{N}^{-1}\left|\tilde{T}_h\right\rangle$, where $\left|\tilde{T}_h\right\rangle$ is the high-order part of the vector:

$$\left|\tilde{T}_h\right\rangle = \left[0,0,0,0,0,0,\tilde{k}_{21},\tilde{k}_{12},\tilde{k}_{22}\right]^\top \tag{14}$$

It could be proven that the above formulation is equivalent to a central moment based KBC model [13,14]. When the shift matrix **N** is a unit matrix, it reduces to the raw moment based KBC [13,14]. Moreover, if all the parameters in the matrix **S** are set equal to βs_2, with the entropic modification coefficient β defined in Ref. [43], the present formulation could further reduce to the original ELBM. With the stabilizing effects of the entropic condition, KBC and ELBM show considerable improvements in numerical stability, with successful applications to multiphase flows [44–46].

Via the Chapman-Enskog analysis, the present ULBM reproduces the incompressible N-S equations in the low-Mach number limit, and the hydrodynamics variables are obtained as,

$$\rho = \sum_i f_i, \quad \rho \mathbf{u} = \sum_i f_i \mathbf{e}_i. \tag{15}$$

Although the above derivations are based on the D2Q9 lattice, the present ULBM framework is compatible with any discrete velocity models (DVMs). The central moment sets corresponding to different DVMs are given in TABLE I, while the three-dimensional central moments are defined as $\tilde{k}_{mnp} = \left\langle f_i \left| (e_{ix} - u_x)^m (e_{iy} - u_y)^n (e_{iy} - u_z)^p \right. \right\rangle$ and the discrete velocities can be found in [5]. The raw moment set is specified for each DVM analogously. Remarkably, it is seen that the central (or raw) moment set for a sub-lattce (e.g, D3Q19) is exactly a subset of the one on the full-lattice (D3Q27). As a result, the transformation matrix and shift matrix ($\mathbf{M}$ and $\mathbf{N}$) and their inverses on a sub-lattice can be directly obtained from the ones on the full-lattice by extracting the corresponding rows and columns. Such a feature enables much better portability across different lattices compared with the orthogonal MRT models [8,47], and makes it much more convenient for users to implement simulations with different lattices and dimensions.

In summary, the SRT, MRT, CLBM, and KBC models can all be unified within the ULBM framework and the relaxations among different collision models are given in TABLE II. Such a framework can incorporate any new developments in forcing schemes, surface tension models, contact angle treatments, boundary conditions, etc. to form a powerful and general LBM. Besides, any improved scheme for any LB collision operator can be ported to other operators within the ULBM framework to facilitate both model development and application. In TABLE II , we also present a comparison of the numerical stability among different models, by gradually increasing the Reynolds number to find the maximum achievable value $\mathrm{Re}_{\max}$ for simulating a 2D double periodic shear flow [48]. The grid is fixed at 128×128, and the stability is determined by running the simulations up to $t = TU / L = 10$ (T=25600 time steps). The Reynolds number is defined as $\mathrm{Re} = UL / \nu$, with the initial velocity magnitude $U = 0.05$. For MRT and CLBM, numerical stability depends on the choice of the tunable parameters. Here, we choose $s_{2b} = 1.6$, $s_3 = 1.2$ and $s_{2b} = 1.8$ for both the models as used by Liu et al [40]. The results suggest that the numerical stability is in ascending order of SRT, MRT, CLBM and KBC for the present settings. We would like to stress that such a conclusion holds for the cases we have tested so far, and a more comprehensive model performance (e.g. stability) assessment is needed in further work under the ULBM framework.

In many fluid systems, the flow is driven by various external or internal forces, which need to be appropriately incorporated into the LB model. By including the discrete lattice effect and using the second-order integration of the change of the distributions (moments) due to the force field, we show a general forcing term can be added on the right-hand side of the ULBM formulation [Eq. (4)], namely [17,38],

$$f_i^*(\mathbf{x},t) = f_i(\mathbf{x},t) - (\mathbf{N}^{-1}\mathbf{M}^{-1}\mathbf{S}\mathbf{M}\mathbf{N})\left[f_i(\mathbf{x},t) - f_i^{eq}(\mathbf{x},t) \right] + \mathbf{N}^{-1}\mathbf{M}^{-1}(\mathbf{I} - \mathbf{S}/2)\mathbf{M}\mathbf{N}\Delta t \left| R_i \right\rangle \tag{17}$$

where R_i is the discrete forcing term. R_i is defined based on the principle that its discrete central moment should be equal to the continuous central moments of R_M,

$$R^M = \frac{(\boldsymbol{\xi} - \mathbf{u}) \cdot \mathbf{F}}{\rho c_s^2} f^M \tag{18}$$

where f^M is the Maxwellian in the continuous particle velocity space $\boldsymbol{\xi}$ and $\mathbf{F}$ is the forcing field imposed on the system. The explicit formulation of R_i is actually a fourth-order Hermit expansion of R^M, as discussed by Huang et al. [39]. Taking the CLBM with the D2Q9 lattice as an example, we have [38],

$$\left|C_i\right\rangle = \mathbf{NM}\left|R_i\right\rangle = [0, F_x, F_y, 0, 0, 0, c_s^2 F_y, c_s^2 F_x, 0]^\top. \tag{19}$$

For other models with different lattices, the forcing term could also be defined based on the above principle. With the redefined post-collision distribution in Eq. (17), the momenta are then computed by,

$$\rho\mathbf{u} = \sum_i f_i \mathbf{e}_i + \Delta t\mathbf{F}/2. \tag{20}$$

We name the forcing scheme under such a principle as the consistent forcing scheme, because the forcing term is reduced to the widely used scheme in MRT-LBM or SRT-LBM, respectively, when the relaxation model is reduced.

To demonstrate the importance of incorporating a consistent forcing scheme, it is instructive to compare the consistent forcing scheme with other schemes where this constraint is not satisfied. We conduct simulations of a single static droplet in a 2D periodic square by CLBM with the consistent forcing scheme (M_p) and three representative schemes in the literature, denoted by M_1 [36], M_2 [15], and M_3 [49], respectively. The original pseudopotential multiphase model is adopted, where the pseudopotential-based interaction force among fluid particles is incorporated by different forcing schemes. As shown in Figure 1, the droplet's stationary shape simulated by the present forcing scheme almost remains circular ($I = 1.0$) when the third-order relation parameter s_3 is varied over a wide range. The droplet shape is measured by a deformation parameter $I = \left|R_{\pi/4} / R_0\right|$, where the subscript denotes the angle between the x-axis and the line along which the radius R is measured. For other three forcing schemes, the deformation parameter varies with s_3. Under certain conditions, an initial circular droplet deforms significantly to be a non-circular (even square) shape, as also demonstrated by the insets. The comparison reaffirms the necessity to impose the consistent constraint on the forcing scheme for the ULBM framework.

3. Results

In this section, we demonstrate the application of the ULBM framework to a variety of multiphase and/or thermal phenomena over a wide range of conditions. Three different problems are considered here to highlight the flexibility and capability afforded by the ULBM framework: the rheology of an emulsion, splashing of a droplet on a liquid film, and dynamics of pool boiling. In response to the different values of the physical parameters involved (Reynolds number, density ratio, viscosity ratio, Rayleigh number, et al), ULBM can selectively use the SRT-LBM, non-orthogonal MRT-LBM, and CLBM, respectively, to balance model performance and computational cost. The insights gained would allow judicial choices of models that are best suited to future simulations, all within the ULBM framework. Moreover, the current limitations of existing models are analyzed and put in context.

3.1 Simulations of emulsion rheology

First, we consider a droplet emulsion system, which consists of dispersed droplets (component 1) in the continuous matrix (component 2). In the experiments [50], the dispersion is stabilized against full phase separation due to the presence of surfactants, which reduce the interfacial energy and prevent droplet coalescence. The microscopic mechanism of the stabilization effect of surfactants can be interpreted at the mesoscopic level using the concept of disjoining pressure from the theory of thin liquid films [51]. The disjoining pressure works as a repulsive force per unit area between approaching interfaces, induced by inter/intra-species interactions, and stabilizes the thin film. It could be conveniently incorporated into the mesoscale LB models

[52–55]. Within the multicomponent pseudopotential model, the key technique is the introduction of a competing mechanism between short-range attractive and mid-range repulsive interactions, within each component, as originally proposed by Benzi et al. [52,53]. For 2D cases, the competing interaction force is written as [52,53],

$$\mathbf{F}_k^c = -G_{k,1}\psi_k(\mathbf{x})\sum_{i=0}^{8} w(|\mathbf{e}_i|^2)\psi_k(\mathbf{x}+\mathbf{e}_i)\mathbf{e}_i - G_{k,2}\psi_k(\mathbf{x})\sum_{j=0}^{24} p(|\mathbf{e}_j|^2)\psi_k(\mathbf{x}+\mathbf{e}_j)\mathbf{e}_j, \tag{21}$$

where $G_{k,1}$ and $G_{k,2}$ are strength coefficients for the short-range (within D2Q9 lattice) and mid-range (up to D2Q25 lattice) interactions for the component k (=1,2), respectively. More details, such as the weights $w(|\mathbf{e}_i|^2)$ and $p(|\mathbf{e}_j|^2)$ and the pseudopotential for each component ψ_k are described in [56]. The inter-species repulsive force between component 1 and 2 is defined as [24,25],

$$\mathbf{F}_k^r = -\rho_k(\mathbf{x})\sum_{\bar{k}} G_{k\bar{k}}\sum_{i=0}^{8} w(|\mathbf{e}_i|^2)\rho_{\bar{k}}(\mathbf{x}+\mathbf{e}_i)\mathbf{e}_i, \tag{22}$$

Incorporating the body force $\mathbf{F}_k^b$, the total force imposed on each species is $\mathbf{F}_k = \mathbf{F}_k^c + \mathbf{F}_k^r + \mathbf{F}_k^b$. Considering that droplet emulsions are usually used in micro-fluidic systems, with the flow mainly in the low-Reynolds number regime, we can select the SRT model within the ULBM framework. The collision step in the SRT model with the forcing term is given as [56],

$$f_{k,i}^*(\mathbf{x},t) = f_{k,i}(\mathbf{x},t) - \frac{1}{\tau_k}\left[f_{k,i}(\mathbf{x},t) - f_{k,i}^{eq}(\rho_k,\mathbf{u}^{eq})\right] + \left(1-\frac{1}{2\tau}\right)\Delta t R_{k,i}(\rho_k,\mathbf{u}^{eq}) \tag{23}$$

where $\mathbf{u}^{eq}$ is the equilibrium velocity for the multi-component mixture [57]. Incorporating the total force into the forcing term $R_{k,i}$ [56], we have

$$R_{k,i} = w(|\mathbf{e}_i|^2)\left[\frac{\mathbf{e}_i - \mathbf{u}^{eq}}{c_s^2} + \frac{(\mathbf{e}_i\cdot\mathbf{u}^{eq})}{c_s^4}\mathbf{e}_i\right]\cdot\mathbf{F}_k \tag{24}$$

The present model is able to achieve a positive disjoining pressure, independent of the viscosity ratio between components 1 and 2. This enables the simulation of highly-packed droplet emulsions under pressure-driven flows [56,58].

The SRT LBM with the new forcing term is then employed to simulate the flow of a concentrated emulsion in a 2D tapered microfluidic channel. Consistent with the experimental condition, the taper has a half-angle of 5° with an extruder of a width of 30 μm, which allows up to tens of droplets to pass through, depending on the droplet radius [50]. The emulsion consists of highly-packed monodisperse water droplets suspended in a fluorinated oil, with a volume fraction up to 85%. In the experiments, a constant inflowing velocity was controlled in the inlet, and the emulsion flowed and settled well into a hexagonally packed crystal, as shown in Figure 2 (a). In the simulations, the emulsion is driven by a constant pressure-gradient (body force), and the key non-dimensional parameters (Reynolds number and Capillary number) are set equal to the experimental values. As a result, the present simulations can well reproduce the pattern in experiments, as seen in Figure 2 (b). The experiments revealed a very interesting spatial-temporal periodicity of dislocation dynamics, which was attributed to the regular T1 event in such an emulsion configuration. As presented in Figure 2 (c), the present simulations also capture the dynamic T1 event involving one pair of diverging droplets (marked by 2 and 4) and another pair of converging droplets (marked by 1 and 3).

3.2 Simulations of droplet splashing

We now consider the problem of droplet splashing on a thin liquid film. Such a phenomenon is observed widely in both nature and technological applications, from a raindrop falling into a pond to spray cooling and coating [59], and the printing process [60]. It is challenging to simulate the droplet splashing process because it usually involves multiphase flows at a large density ratio, high Reynolds, and Weber numbers.

Such a process could be described by the single-component pseudopotential multiphase LB model, where the forcing term is written as,

$$\mathbf{F}_{\text{int}} = -G\psi(\mathbf{x})\sum_i w(|\mathbf{e}_i|^2)\psi(\mathbf{x}+\mathbf{e}_i\Delta t)\mathbf{e}_i \tag{25}$$

In the above, G controls the interaction strength, ψ is the pseudopotential function, and $w(|\mathbf{e}_i|^2)$ is the normalized weight. To achieve a wider parameter range while retaining high computational efficiency, the non-orthogonal MRT collision operator is selected as a reduced form of ULBM. In the non-orthogonal MRT model, the collision step can be written as [42],

$$f_i^*(\mathbf{x},t) = f_i(\mathbf{x},t) - (\mathbf{M}^{-1}\mathbf{S}\mathbf{M})\left[f_i(\mathbf{x},t) - f_i^{eq}(\mathbf{x},t)\right] + \Delta t\mathbf{M}^{-1}(\mathbf{I}-\mathbf{S}/2)\mathbf{M}\left|R_i\right\rangle \tag{26}$$

where the third term on the right-hand side is the forcing contribution. Using the D3Q19 lattice model and the moment set in Table I, the explicit formulation of the forcing term in the raw moment space is written as,

$$\left|\tilde{F}_i\right\rangle = \mathbf{M}\left|R_i\right\rangle = [0, F_x, F_y, F_z, 2\mathbf{F}\cdot\mathbf{u}, 2(F_xu_x - F_yu_y), 2(F_xu_x - F_zu_z), F_xu_y + F_yu_x, F_xu_z + F_zu_x, F_yu_z + F_zu_y, F_xc_s^2, F_xc_s^2, F_yc_s^2, F_zc_s^2, F_yc_s^2, F_zc_s^2, 2c_s^2(F_xu_x + F_yu_y), 2c_s^2(F_xu_x + F_zu_z), 2c_s^2(F_yu_y + F_zu_z)]^\top \tag{27}$$

To incorporate the realistic equation of state (EOS) for the simulation of large density ratio multiphase flows, the square-root-form pseudopotential [61] $\psi = \sqrt{2(p_{EOS} - \rho c_s^2)/Gc^2}$ is used in this work, where p_{EOS} is the pressure in the EOS. With the square-root-form EOS, some elements in the forcing term need to be slightly modified to achieve thermodynamic consistency and tunable surface tension [31,32]. Alternatively, the thermodynamic inconsistency of the pseudopotential model could be addressed by a sophisticated two-range interaction scheme [62,63] instead of the single-range interaction in Eq. (25). In the present non-orthogonal MRT model, the modifications are given as [42],

$$\begin{aligned}
&\tilde{F}_4^{'} = \tilde{F}_4 + \frac{6\sigma|\mathbf{F}_{\text{int}}|^2}{\psi^2(s_{2b}^{-1}-0.5)\delta t} + \frac{4(Q_{xx}+Q_{yy}+Q_{zz})}{5(s_{2b}^{-1}-0.5)\Delta t}, \tilde{F}_5^{'} = \tilde{F}_5 - \frac{(Q_{xx}-Q_{yy})}{(s_2^{-1}-0.5)\Delta t}, \tilde{F}_6^{'} = \tilde{F}_6 - \frac{(Q_{xx}-Q_{zz})}{(s_2^{-1}-0.5)\Delta t} \\
&\tilde{F}_7^{'} = \tilde{F}_7 - \frac{Q_{xy}}{(s_2^{-1}-0.5)\Delta t}, \tilde{F}_8^{'} = \tilde{F}_8 - \frac{Q_{xz}}{(s_2^{-1}-0.5)\Delta t}, \tilde{F}_9^{'} = \tilde{F}_9 - \frac{Q_{yz}}{(s_2^{-1}-0.5)\Delta t},
\end{aligned} \tag{28}$$

where the tunable parameter σ restores the thermodynamic consistency. The variable $Q_{\alpha\beta}$ is given by [32],

$$Q_{\alpha\beta} = \kappa\frac{G}{2}\psi(\mathbf{x})\sum_i w(|\mathbf{e}_i|^2)\left[\psi(\mathbf{x}+\mathbf{e}_i\Delta t) - \psi(\mathbf{x})\right]\mathrm{e}_{i\alpha}e_{i\beta}, \tag{29}$$

where the parameter κ is used to tune the surface tension.

In the following, we adopt the above non-orthogonal MRT LBM model to simulate a droplet splashing on a liquid film. Firstly, following the experimental setup in [64], we simulate a water droplet impacting a thin water film. The initial diameter of the water droplet is 3.15 mm and the ratio of liquid film depth to droplet initial diameter is 0.22. The dynamics of the impacting droplet is displayed in Figure 3, where the dimensionless time T^* is defined as $T^* = u_0T/D_0$, u_0 is the impacting speed, T is the time step and D_0 is the droplet initial diameter. The simulation and experiment results are qualitatively compared for two Weber numbers. Figure 3(a) shows the We = 249 case, and Figure 3(b) represents the We = 328 case. To simulate the realistic situation, we set the density ratio as 1000 and Re more than 5000 for all cases. Additionally, in order to capture all the features of droplet splashing as well as ensuring numerical stability, the simulation is conducted at a very high resolution with the droplet radius fixed at 80 lattices. The simulation domain in x, y, and z directions extends to 14, 14, and 5 times of the droplet radius, respectively, which leads to the total grid numbers over 500 million. As seen in Figures 3(a) and 3(b), the simulation (blue snapshots) and experimental results (grey snapshots) are in good agreement. Same to the experiment phenomena, for the lower We case (Figure 3(a)), only the formation of the liquid crown is observed in the simulation. For the higher We case (Figure 3(b)), both the liquid crown and

droplet "pearls" can be observed. Finally, we provide a prediction at a much higher We case (We=540) in Figure 3(c), which presents the dynamic process of crown formation is accelerated as We is increased.

3.3 Simulations of phase change and boiling dynamics

Finally, the ULBM framework is employed to simulate the phase-change pool boiling process. Boiling is a highly efficient heat transfer process, which is routinely observed in our daily life and in many power plants. Boiling is an extremely complex process, including bubble dynamics (nucleation, growth, departure, deformation, coalescence, and breakup), phase-change heat transfer, and even turbulence. Usually, with the increase of the wall superheat, different boiling regimes would appear [65,66]: nucleate boiling (discrete bubble region and mushroom bubble region), transition boiling, and film boiling.

In this subsection, we consider the simulation of the 3D pool boiling process, where vapor bubbles and heated liquid are driven by the gravity-induced buoyancy force. To simulate such a highly unsteady multiphase and thermodynamic phase transition process, a robust and stable method is required. Within the ULBM, the multiphase CLBM has superior stability and is thus chosen for the simulation. To model the multiphase flow field, the single-component pseudopotential is adopted and the interaction force is defined in Eq. (25). Inspired by the method of Li et al. [31], the forcing term is slightly modified to achieve thermodynamic consistency. For the D3Q19 lattice model and the moment set in Table I, the forcing term is given as [48],

$$\left|C_i\right\rangle = [0, F_x, F_y, F_z, \eta, 0, 0, 0, 0, 0, F_x c_s^2, F_x c_s^2, F_y c_s^2, F_z c_s^2, F_y c_s^2, F_z c_s^2, 0, 0, 0]^{\top}. \tag{30}$$

where η is defined as,

$$\eta = \frac{6\sigma \left|\mathbf{F}_{\text{int}}\right|^2}{\psi^2 (s_{2b}^{-1} - 0.5)\delta t}, \tag{31}$$

in which σ is used to adjust the mechanical stability condition.

The temperature equation of the liquid-vapor phase-change process can be written as [68],

$$\frac{\partial T}{\partial t} = -\mathbf{u}\cdot\nabla T + \frac{1}{\rho c_v}\left(\lambda \nabla^2 T + \nabla\lambda\cdot\nabla T\right) - \frac{T}{\rho c_v}\left(\frac{\partial p_{\text{EOS}}}{\partial T}\right)_{\rho} \nabla\cdot\mathbf{u}, \tag{32}$$

where c_v is the specific heat at constant volume and λ is the thermal conductivity. Previously, a hybrid LB – finite difference scheme was proposed by Li et al. [68] to simulate the boiling phenomenon. The same approach is adopted by Fei et al. [67], except that the flow field is solved by the above CLBM. The finite difference method is used to solve the temperature field [Eq. (32)], and the thermal and hydrodynamic fields are coupled via a non-ideal equation of state.

The boiling simulation is carried out in a computational box of $600\Delta x \times 600\Delta x \times 300\Delta x$, with periodic boundary conditions along the x and y directions and the non-slip boundary conditions at $z = 0$ and $z = 600\Delta x$. The system is heated by a constant wall superheat ($\Delta T = T_b - T_s$), where T_b and T_s are the temperatures of the bottom wall and the saturation temperature, respectively. The bottom wall is hydrophilic with a static contact angle $\theta \approx 50^{\circ}$. Initially, the lower part of the system ($z < 360\Delta x$) is set as the saturated liquid ($\rho = \rho_l, T = T_s$), and the upper part is set as the saturated vapor ($\rho = \rho_v, T = T_s$). To trigger the nucleation, small temperature disturbances are added in the grid layer near the wall, i.e., $T = T_s + \delta T$. By gradually increasing the wall superheat, boiling simulations at different Jacob numbers (Ja) are conducted. Figure 4 (a)-(d) shows the snapshots of the pool boiling process at $Ja = 0.220$, $Ja = 0.283$, $Ja = 0.441$ and $Ja = 0.448$, respectively. In figure 4 (a), it can be seen that numerous bubbles are continuously formed through nucleation. These bubbles then grow, depart the hot solid surface, and rise through the liquid pool almost independently, either reaching the pool surface or breaking up before that. The bubbles carry hot fluids from the wall and facilitate heat transfer to the fluids. This case features the nucleate boiling regime. Compared with panel (a), the bubbles in panel (b) are larger and more likely to merge when they depart and rise, although both cases show very efficient heat transfer. The case at $Ja = 0.283$ is in the mushroom bubble region of the nucleate boiling regime. With the further increase of superheat, the transition boiling regime and film boiling regime are

reproduced, as shown in Figure 4 (c) and (d), respectively. In total, up to hundreds of spontaneously generated bubbles are included in this 3D simulation of pool boiling, providing both unprecedented insights into the physics of boiling and valuable statistical data.

4. Conclusion

In this work, a unified lattice Boltzmann model (ULBM) framework is developed, which seamlessly integrates the widely used existing lattice Boltzmann models (SRT, MRT, Cascaded, Entropic, and KBC). In the ULBM framework, a transformation matrix is constructed to transform the particle distribution functions into their raw moments, a shift matrix converts the raw moments into central moments, and the entropic condition is incorporated to dynamically optimize the relaxation parameters at each lattice site in every time step. In this way, we not only put the popular LB models in a general mathematical framework but also clarifies the relations among them. The ULBM framework is generic, in the sense that it is applicable to all LB models designed specifically for incompressible/compressible, single-phase/multiphase, athermal/thermal, laminar/turbulent, nonreactive/reactive flows. As a result, ULBM makes LB codes and models much more portable. For example, an LB code can easily incorporate different existing models into the same coding structure. Equally, any improved model constructed for one collision operator can be easily adopted by other operators. Finally, strengths in different LB models (e.g. forcing schemes) can be integrated to create more powerful models.

The validity and usefulness of the new ULBM are demonstrated through three different multiphase problems: 1) a pressure-driven two-species highly-packed emulsion in a two-dimensional tapered channel, 2) a droplet splashing on a thin water film at high Reynolds and Weber numbers and 3) a large-scale three-dimensional pool boiling process. It is demonstrated that within the ULBM framework, it is convenient to switch between LB models and treatments, allowing judicial choices to suit the problems under investigation. Model comparisons are also made easy. As an additional outcome, we show that with the recent developments in multiphase LB models put under the ULBM framework, a wide range of complex multiphase flows, from single-species to multi-species multiphase flows, and even with phase-change heat transfer can be simulated using realistic values of physical parameters.

The power of the ULBM framework will be explored in future work. In addition to multiphase LB models, the diverse LB models for compressible, multicomponent, thermal, turbulent, and reactive flows, respectively, can be assessed within a unified framework. A complete map of the stability and validity of each model can be constructed to facilitate judicial choices of models in terms of accuracy, reliability, and computational cost. Moreover, any new LB model or numerical method for a particular problem can be rapidly and conveniently extended to other problems.

Additional Information

Funding Statement

Funding from the EPSRC project “UK Consortium on Mesoscale Engineering Sciences (UKCOMES)” (Grant Nos. EP/R029598/1 and EP/V001531/1) is gratefully acknowledged.

Data Accessibility

Supporting data are available on request.

Competing Interests

We have no competing interests.

Authors' Contributions

Kai H. Luo and Linlin Fei conceptualized the models and ideas for the ULBM framework. Linlin Fei further developed the code. Linlin Fei and Geng Wang conducted the simulations. Kai H. Luo supervised the project. All authors contributed to the writing of the paper.

References

1. Qian Y-H, Succi S, Orszag SA. 1995 Recent advances in lattice Boltzmann computing. In *Annual*

reviews of computational physics III, pp. 195–242. World Scientific.
2. Succi S. 2001 *The lattice Boltzmann equation: for fluid dynamics and beyond*. Oxford university press.
3. Succi S. 2018 *The Lattice Boltzmann Equation: For Complex States of Flowing Matter*. Oxford university press.
4. Li Q, Luo KH, Kang Q, He YL, Chen Q, Liu Q. 2016 Lattice Boltzmann methods for multiphase flow and phase-change heat transfer. *Prog. Energy Combust. Sci.* **52**, 62–105. (doi:10.1016/j.pecs.2015.10.001)
5. Aidun CK, Clausen JR. 2010 Lattice-Boltzmann Method for Complex Flows. *Annu. Rev. Fluid Mech.* **42**, 439–472. (doi:10.1146/annurev-fluid-121108-145519)
6. Qian Y-H, d'Humières D, Lallemand P. 1992 Lattice BGK models for Navier-Stokes equation. *EPL (Europhysics Lett.* **17**, 479.
7. Ginzburg I, d'Humières D. 2003 Multireflection boundary conditions for lattice Boltzmann models. *Phys. Rev. E* **68**, 066614. (doi:10.1103/PhysRevE.68.066614)
8. Lallemand P, Luo L-S. 2000 Theory of the lattice Boltzmann method: Dispersion, dissipation, isotropy, Galilean invariance, and stability. *Phys. Rev. E* **61**, 6546–6562. (doi:10.1103/PhysRevE.61.6546)
9. Guo Z, Zheng C. 2008 Analysis of lattice Boltzmann equation for microscale gas flows: Relaxation times, boundary conditions and the Knudsen layer. *Int. J. Comut. Fluid Dyn.* **22**, 465–473. (doi:10.1080/10618560802253100)
10. Chiappini D, Sbragaglia M, Xue X, Falcucci G. 2019 Hydrodynamic behavior of the pseudopotential lattice Boltzmann method for interfacial flows. *Phys. Rev. E* **99**, 53305. (doi:10.1103/PhysRevE.99.053305)
11. Geier M, Greiner A, Korvink JG. 2006 Cascaded digital lattice Boltzmann automata for high Reynolds number flow. *Phys. Rev. E - Stat. Nonlinear, Soft Matter Phys.* **73**, 1–10. (doi:10.1103/PhysRevE.73.066705)
12. Lycett-Brown D, Luo KH. 2016 Cascaded lattice Boltzmann method with improved forcing scheme for large-density-ratio multiphase flow at high Reynolds and Weber numbers. *Phys. Rev. E* **94**, 1–20. (doi:10.1103/PhysRevE.94.053313)
13. Karlin I V., Bösch F, Chikatamarla SS. 2014 Gibbs' principle for the lattice-kinetic theory of fluid dynamics. *Phys. Rev. E - Stat. Nonlinear, Soft Matter Phys.* **90**, 1–5. (doi:10.1103/PhysRevE.90.031302)
14. Bösch F, Chikatamarla SS, Karlin I. 2015 Entropic multi-relaxation lattice Boltzmann scheme for turbulent flows, *Phys. Rev. E* **92**, 043309, 1-15. (doi:10.1103/PhysRevE.92.043309)
15. Lycett-Brown D, Luo KH. 2014 Multiphase cascaded lattice Boltzmann method. *Comput. Math. Appl.* **67**, 350–362. (doi:10.1016/j.camwa.2013.08.033)
16. De Rosis A. 2017 Nonorthogonal central-moments-based lattice Boltzmann scheme in three dimensions. *Phys. Rev. E* **95**, 1–16. (doi:10.1103/PhysRevE.95.013310)
17. Fei L, Luo KH, Li Q. 2018 Three-dimensional cascaded lattice Boltzmann method: Improved implementation and consistent forcing scheme. *Phys. Rev. E* **97**, **053309**, 1–12. (doi:10.1103/PhysRevE.97.053309)
18. Gunstensen AK, Rothman DH, Zaleski S, Zanetti G. 1991 Lattice Boltzmann model of immiscible fluids. *Phys. Rev. A* **43**, 4320.
19. Grunau D, Chen S, Eggert K. 1993 A lattice Boltzmann model for multiphase fluid flows. *Phys. Fluids A Fluid Dyn.* **5**, 2557–2562.
20. He X, Chen S, Zhang R. 1999 A lattice Boltzmann scheme for incompressible multiphase flow and its application in simulation of Rayleigh-Taylor instability. *J. Comput. Phys.* **152**, 642–663.
21. Inamuro T, Ogata T, Tajima S, Konishi N. 2004 A lattice Boltzmann method for incompressible two-phase flows with large density differences. *J. Comput. Phys.* **198**, 628–644.
22. Swift MR, Osborn WR, Yeomans JM. 1995 Lattice Boltzmann simulation of nonideal fluids. *Phys. Rev. Lett.* **75**, 830.
23. Swift MR, Orlandini E, Osborn WR, Yeomans JM. 1996 Lattice Boltzmann simulations of liquid-gas and binary fluid systems. *Phys. Rev. E* **54**, 5041.

24. Shan X, Chen H. 1993 Lattice Boltzmann model for simulating flows with multi phases and components. *Phys. Rev. E* **47**, 1815–1819. (doi:10.1103/PhysRevE.47.1815)
25. Shan XW, Chen HD. 1994 Simulation of Nonideal Gases and Liquid-Gas Phase-Transitions by the Lattice Boltzmann-Equation. *Phys. Rev. E* **49**, 2941–2948. (doi:10.1103/PhysRevE.49.2941)
26. Succi S. 2015 Lattice Boltzmann 2038. *EPL (Europhysics Lett.* **109**, 50001. (doi:10.1209/0295-5075/109/50001)
27. Shan X. 2006 Analysis and reduction of the spurious current in a class of multiphase lattice Boltzmann models. *Phys. Rev. E - Stat. Nonlinear, Soft Matter Phys.* **73**, 6–9. (doi:10.1103/PhysRevE.73.047701)
28. Sbragaglia M, Benzi R, Biferale L, Succi S, Sugiyama K, Toschi F. 2007 Generalized lattice Boltzmann method with multirange pseudopotential. *Phys. Rev. E - Stat. Nonlinear, Soft Matter Phys.* **75**, 1–13. (doi:10.1103/PhysRevE.75.026702)
29. Huang H, Krafczyk M, Lu X. 2011 Forcing term in single-phase and Shan-Chen-type multiphase lattice Boltzmann models. *Phys. Rev. E - Stat. Nonlinear, Soft Matter Phys.* **84**, 1–15. (doi:10.1103/PhysRevE.84.046710)
30. Li Q, Luo KH, Li XJ. 2012 Forcing scheme in pseudopotential lattice Boltzmann model for multiphase flows. *Phys. Rev. E - Stat. Nonlinear, Soft Matter Phys.* **86**, 1–9. (doi:10.1103/PhysRevE.86.016709)
31. Li Q, Luo KH, Li XJ. 2013 Lattice Boltzmann modeling of multiphase flows at large density ratio with an improved pseudopotential model. *Phys. Rev. E - Stat. Nonlinear, Soft Matter Phys.* **87**. (doi:10.1103/PhysRevE.87.053301)
32. Li Q, Luo KH. 2013 Achieving tunable surface tension in the pseudopotential lattice Boltzmann modeling of multiphase flows. *Phys. Rev. E - Stat. Nonlinear, Soft Matter Phys.* **88**, 1–10. (doi:10.1103/PhysRevE.88.053307)
33. Lycett-Brown D, Luo KH. 2015 Improved forcing scheme in pseudopotential lattice Boltzmann methods for multiphase flow at arbitrarily high density ratios. *Phys. Rev. E - Stat. Nonlinear, Soft Matter Phys.* **91**. (doi:10.1103/PhysRevE.91.023305)
34. Li Q, Luo KH, Kang QJ, Chen Q. 2014 Contact angles in the pseudopotential lattice Boltzmann modeling of wetting. *Phys. Rev. E - Stat. Nonlinear, Soft Matter Phys.* **90**, 1–9. (doi:10.1103/PhysRevE.90.053301)
35. Li Q, Yu Y, Luo KH. 2019 PHYSICAL REVIEW E 100 , 053313 (2019) Implementation of contact angles in pseudopotential lattice Boltzmann simulations with curved boundaries. *Phys. Rev. E* **100**, **053313**, 1–12. (doi:10.1103/PhysRevE.100.053313)
36. Premnath KN, Banerjee S. 2009 Incorporating forcing terms in cascaded lattice Boltzmann approach by method of central moments. *Phys. Rev. E - Stat. Nonlinear, Soft Matter Phys.* **80**. (doi:10.1103/PhysRevE.80.036702)
37. Karlin I, Asinari P. 2010 Factorization symmetry in the lattice Boltzmann method. *Phys. A Stat. Mech. its Appl.* **389**, 1530–1548. (doi:10.1016/j.physa.2009.12.032)
38. Fei L, Luo KH. 2017 Consistent forcing scheme in the cascaded lattice Boltzmann method. *Phys. Rev. E* **96**, 053307. (doi:10.1103/PhysRevE.96.053307)
39. Huang R, Wu H, Adams NA. 2018 Eliminating cubic terms in the pseudopotential lattice Boltzmann model for multiphase flow. *Phys. Rev. E* **97**, 1–13. (doi:10.1103/PhysRevE.97.053308)
40. Liu Q, He YL, Li D, Li Q. 2016 Non-orthogonal multiple-relaxation-time lattice Boltzmann method for incompressible thermal flows. *Int. J. Heat Mass Transf.* **102**, 1334–1344. (doi:10.1016/j.ijheatmasstransfer.2016.06.029)
41. Li Q, Du DH, Fei LL, Luo KH. 2019 Three-dimensional non-orthogonal MRT pseudopotential lattice Boltzmann model for multiphase flows. *Computers & Fluids* **186**, 128–140. (doi:10.1016/j.compfluid.2019.04.014)
42. Fei L, Du J, Luo KH, Succi S. 2019 Modeling realistic multiphase flows using a non-orthogonal multiple-relaxation-time lattice Boltzmann method Modeling realistic multiphase flows using a

non-orthogonal multiple-relaxation-time lattice Boltzmann method. *Phys. Fluids* **042105**. (doi:10.1063/1.5087266)
43. Karlin I V, Ferrante A, Öttinger HC. 1999 Perfect entropy functions of the Lattice Boltzmann method. *Europhys. Lett.* **47**, 182–188. (doi:10.1209/epl/i1999-00370-1)
44. Montessori A, Prestininzi P, La Rocca M, Succi S. 2017 Entropic lattice pseudo-potentials for multiphase flow simulations at high Weber and Reynolds numbers. *Phys. Fluids* **29**. (doi:10.1063/1.5001253)
45. Bösch F, Dorschner B, Karlin I. 2018 Entropic multi-relaxation free-energy lattice Boltzmann model for two-phase flows. *EPL* **122**. (doi:10.1209/0295-5075/122/14002)
46. Lauricella M, Melchionna S, Montessori A, Pisignano D, Pontrelli G, Succi S. 2018 Entropic lattice Boltzmann model for charged leaky dielectric multiphase fluids in electrified jets. *Phys. Rev. E* **97**, 33308.
47. d'Humieres D, Ginzburg I, Krafczyk M, Lallemand P, Luo L-S. 2002 Multiple-relaxation-time lattice Boltzmann models in three dimensions. *Philos. Trans. R. Soc. A Math. Phys. Eng. Sci.* **360**, 437–451. (doi:10.1098/rsta.2001.0955)
48. Minion ML, Brown DL. 1997 Performance of under-resolved two-dimensional incompressible flow simulations, II. *J. Comput. Phys.* **138**, 734–765.
49. De Rosis A. 2017 Alternative formulation to incorporate forcing terms in a lattice Boltzmann scheme with central moments. *Phys. Rev. E* **95**, 1–8. (doi:10.1103/PhysRevE.95.023311)
50. Gai Y, Min C, Cai W, Tang SKY. 2016 Spatiotemporal periodicity of dislocation dynamics in a two-dimensional microfluidic crystal flowing in a tapered channel. *Proc. Natl. Acad. Sci. U. S. A.* 113, 1–6. (doi:10.1073/pnas.1606601113)
51. Derjaguin B V, Churaev N V. 1978 On the question of determining the concept of disjoining pressure and its role in the equilibrium and flow of thin films. *J. Colloid Interface Sci.* **66**, 389–398.
52. Benzi R, Chibbaro S, Succi S. 2009 Mesoscopic lattice Boltzmann modeling of flowing soft systems. *Phys. Rev. Lett.* **102**, 2–5. (doi:10.1103/PhysRevLett.102.026002)
53. Benzi R, Sbragaglia M, Succi S, Bernaschi M, Chibbaro S. 2009 Mesoscopic lattice Boltzmann modeling of soft-glassy systems: Theory and simulations. *J. Chem. Phys.* **131**. (doi:10.1063/1.3216105)
54. Montessori A, Lauricella M, Tirelli N, Succi S. 2019 Mesoscale modelling of near-contact interactions for complex flowing interfaces. *J. Fluid Mech.* **872**, 327–347.
55. Montessori A, Lauricella M, Tiribocchi A, Succi S. 2019 Modeling pattern formation in soft flowing crystals. *Phys. Rev. Fluids* **4**, 72201.
56. Fei L, Scagliarini A, Montessori A, Lauricella M, Succi S, Luo KH. 2018 Mesoscopic model for soft flowing systems with tunable viscosity ratio. *Phys. Rev. Fluids* **3**, **104304**, 1–18. (doi:10.1103/PhysRevFluids.3.104304)
57. Shan X, Doolen G. 1995 Multicomponent lattice-Boltzmann model with interparticle interaction. *J. Stat. Phys.* **81**, 379–393. (doi:10.1007/BF02179985)
58. Fei L, Scagliarini A, Luo KH. 2020 Soft Matter Discrete fluidization of dense monodisperse emulsions in neutral wetting microchannels †. *Soft Matter* **16**, 651–658. (doi:10.1039/c9sm02331c)
59. Li H, Zhao Y, Yuan X. 2013 Facile preparation of superhydrophobic coating by spraying a fluorinated acrylic random copolymer micelle solution. *Soft Matter* **9**, 1005–1009.
60. Willis DA, Grosu V. 2005 Microdroplet deposition by laser-induced forward transfer. *Appl. Phys. Lett.* **86**, 244103.
61. Yuan P, Schaefer L. 2006 Equations of state in a lattice Boltzmann model. *Phys. Fluids* **18**. (doi:10.1063/1.2187070)
62. Falcucci G, Bella G, Chiatti G, Chibbaro S, Sbragaglia M, Succi S. 2007 Lattice Boltzmann models with mid-range interactions. *Commun. Comput. Phys.* **2**, 1071–1084.
63. Falcucci G, Ubertini S, Succi S. 2010 Lattice Boltzmann simulations of phase-separating flows at large density ratios: The case of doubly-attractive pseudo-potentials. *Soft Matter* **6**, 4357–4365. (doi:10.1039/c002974b)
64. Che Z, Matar OK. 2017 Impact of Droplets on Liquid Films in the Presence of Surfactant. *Langmuir*

33, 12140–12148. (doi:10.1021/acs.langmuir.7b01901)
65. Nukiyama S. 1934 The Maximum and Minimum Values of the Heat Q Transmitted from Metal to Boiling Water under Atmospheric Pressure. *J. Japan Soc. Mech. Engrs* **37**, 367–374.
66. Dhir VK. 1998 Boiling heat transfer. *Annu. Rev. Fluid Mech.* **30**, 365–401.
67. Fei L, Yang J, Chen Y, Mo H, Luo KH. 2020 Mesoscopic simulation of three-dimensional pool boiling based on a phase-change cascaded lattice Boltzmann method Mesoscopic simulation of three-dimensional pool boiling based on a phase-change cascaded lattice Boltzmann method. *Phys. Fluids* **32**, **103312**. (doi:10.1063/5.0023639)
68. Li Q, Kang QJ, Francois MM, He YL, Luo KH. 2015 Lattice Boltzmann modeling of boiling heat transfer: The boiling curve and the effects of wettability. *Int. J. Heat Mass Transf.* **85**, 787–796. (doi:10.1016/j.ijheatmasstransfer.2015.01.136)
69. Fei L, Luo KH, Lin C, Li Q. 2017 Modeling incompressible thermal flows using a central-moment-based lattice Boltzmann method. *Int. J. Heat Mass Transf.* **120**, 624–634. (doi:10.1016/j.ijheatmasstransfer.2017.12.052)

Tables

TABLE I. Central moment sets for different DVMs/lattices.

DVMs	Central moment sets
D3Q27 [17,42]	$\left\|\tilde{T}_i\right\rangle = [\tilde{k}_{000}, \tilde{k}_{100}, \tilde{k}_{010}, \tilde{k}_{001}, \tilde{k}_{200}+\tilde{k}_{020}+\tilde{k}_{002}, \tilde{k}_{200}-\tilde{k}_{020}, \tilde{k}_{200}-\tilde{k}_{002}, \tilde{k}_{110}, \tilde{k}_{101}, \tilde{k}_{011}, \tilde{k}_{120}, \tilde{k}_{102}, \tilde{k}_{210}, \tilde{k}_{201}, \tilde{k}_{012}, \tilde{k}_{021}, \tilde{k}_{111}, \tilde{k}_{220}, \tilde{k}_{202}, \tilde{k}_{022}, \tilde{k}_{211}, \tilde{k}_{121}, \tilde{k}_{112}, \tilde{k}_{122}, \tilde{k}_{212}, \tilde{k}_{221}, \tilde{k}_{222}]^\top$
D3Q19 [17,42]	$\left\|\tilde{T}_i\right\rangle = [\tilde{k}_{000}, \tilde{k}_{100}, \tilde{k}_{010}, \tilde{k}_{001}, \tilde{k}_{200}+\tilde{k}_{020}+\tilde{k}_{002}, \tilde{k}_{200}-\tilde{k}_{020}, \tilde{k}_{200}-\tilde{k}_{002}, \tilde{k}_{110}, \tilde{k}_{101}, \tilde{k}_{011}, \tilde{k}_{120}, \tilde{k}_{102}, \tilde{k}_{210}, \tilde{k}_{201}, \tilde{k}_{012}, \tilde{k}_{021}, \tilde{k}_{220}, \tilde{k}_{202}, \tilde{k}_{022}]^\top$
D2Q9 [38]	$\left\|\tilde{T}_i\right\rangle = \left[\tilde{k}_{00}, \tilde{k}_{10}, \tilde{k}_{01}, \tilde{k}_{20}+\tilde{k}_{02}, \tilde{k}_{20}-\tilde{k}_{02}, \tilde{k}_{11}, \tilde{k}_{21}, \tilde{k}_{12}, \tilde{k}_{22}\right]^\top$
D2Q5 [69]	$\left\|\tilde{T}_i\right\rangle = \left[\tilde{k}_{00}, \tilde{k}_{10}, \tilde{k}_{01}, \tilde{k}_{20}+\tilde{k}_{02}, \tilde{k}_{20}-\tilde{k}_{02}\right]^\top$

TABLE II. Comparisons among different collision models for the D2Q9 lattice, within the ULBM framework in Eq. (4). In the table, "-" means that the specified matrix is not needed in the implementation. The maximum achievable Reynolds number $\mathrm{Re}_{\max}$ is obtained by gradually increasing the Reynolds number until numerical instability happens, based on a 2D double periodic shear flow case.

Models	$\mathbf{M}$	$\mathbf{N}$	$\mathbf{S}$	$\mathrm{Re}_{\max}$
SRT	-	-	$\mathbf{S} = s_2\mathbf{I}$	2×10^4
MRT	As usual	$\mathbf{N} = \mathbf{I}$	$\mathbf{S} = \mathrm{diag}(1.0,1.0,1.0,s_{2b},s_2,s_2,s_3,s_3,s_4)$	1×10^5
CLBM	As usual	As usual	$\mathbf{S} = \mathrm{diag}(1.0,1.0,1.0,s_{2b},s_2,s_2,s_3,s_3,s_4)$	1×10^8
KBC	As usual	As usual	$\mathbf{S} = \mathrm{diag}(1.0,1.0,1.0,s_2,s_2,s_2,\gamma s_2,\gamma s_2,\gamma s_2)$	infinite

Figures

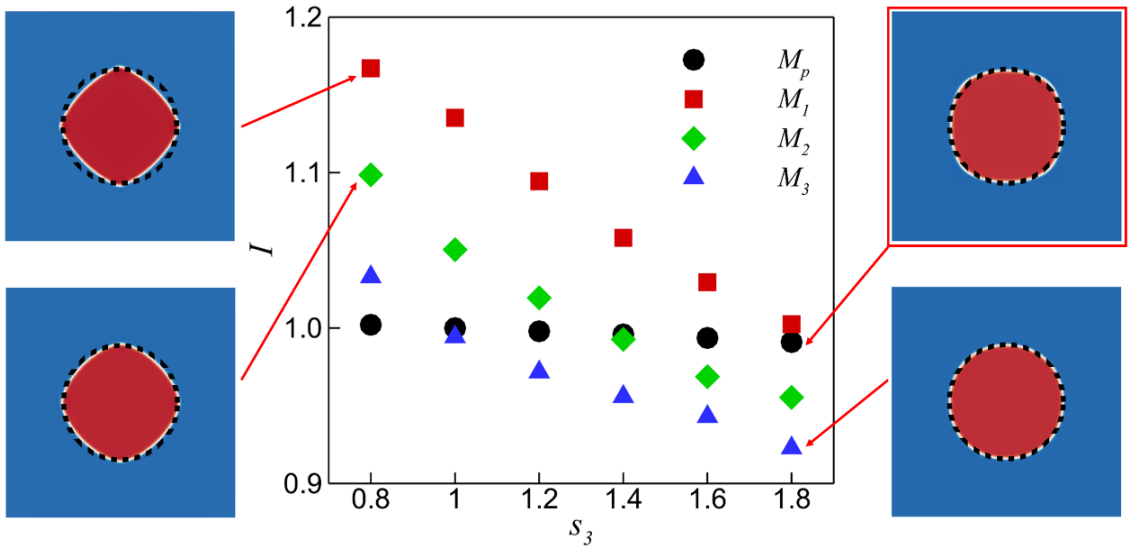

Figure 1: Simulation of a static droplet by ULBM (CLBM option with the consistent forcing scheme M_p) and other three schemes, denoted by M_1 [36], M_2 [15], and M_3 [49]. The exponential pseudopotential is used, i.e., $\psi(\rho) = \exp(-1/\rho)$ and the interaction strength parameter is $G = 10/3$, which leads to a density ratio of 8 and interface thickness of 3 lattice spacings. The main panel shows the change of the deformation parameter $I = |R_{\pi/4} / R_0|$ with the third-order relaxation parameter s_3, where $I = 1.0$ denotes a perfect circular shape. The insets present four representative density contours by the four forcing schemes, respectively. The additional dashed circle is the theoretical location of the droplet. It is clearly seen that the consistent forcing scheme [38] always produces circular droplets, while other schemes result in s_3-dependent droplet deformations.

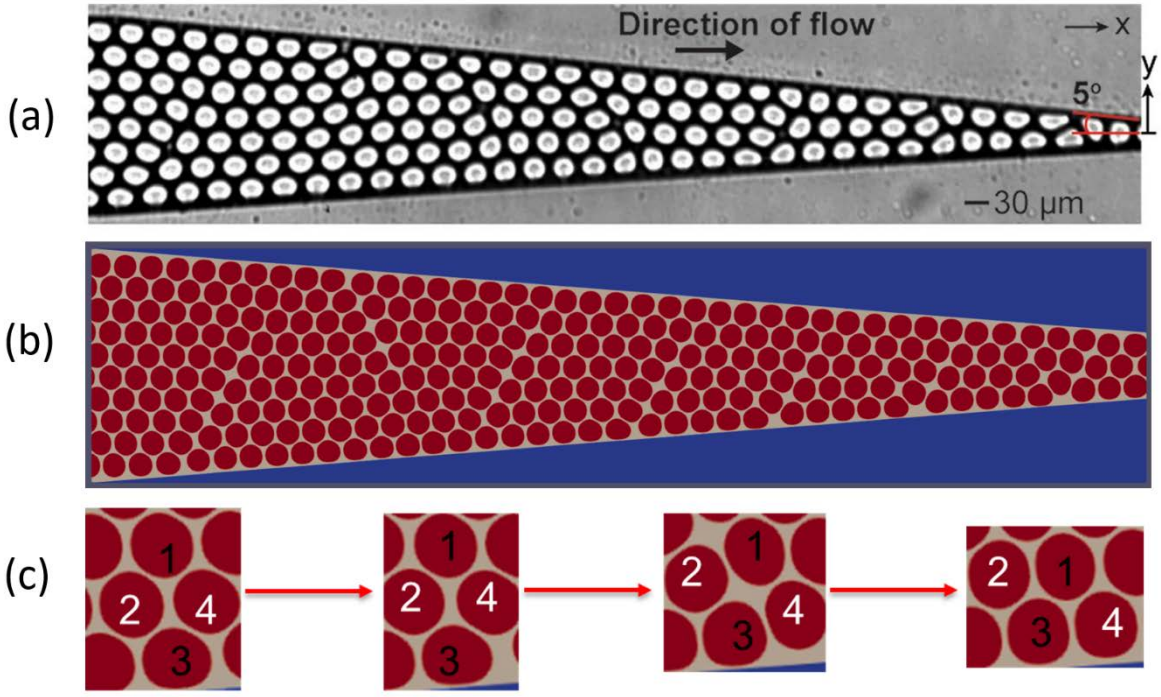

Figure 2: Simulation (ULBM with the SRT multi-species option) of highly-packed monodisperse droplet emulsions (volume fraction up to 85%) in a 2D tapered channel: (a) the flowing pattern in the experiments [50] and (b) the flow pattern in the present simulation. The emulsions arrange automatically into a hexagonally packed crystal and flow with a regular spatial-temporal periodicity of dislocation dynamics. Such a dynamic

process consists of numerous periodic T1 events, which involves one pair of diverging droplets (by 2 and 4) and another pair of converging droplets (marked 1 and 3), as confirmed in our simulations in Panel (c).

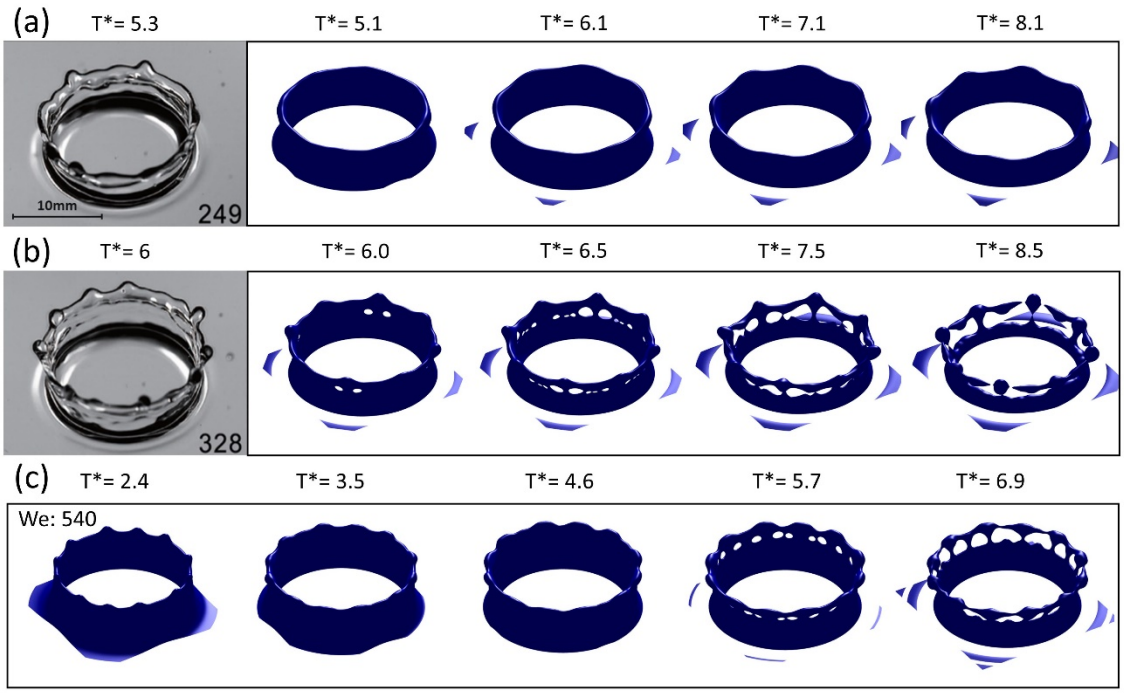

Figure 3: 3D simulation (ULBM with the non-orthogonal MRT multiphase option) of a water droplet splashing on a thin water film at a density ratio of 1000 and a Reynolds number of 5000 (based on the droplet diameter of 160, impacting velocity of 0.08 and kinematic viscosity of 0.0025, in lattice units). The Weber number (We) is increased by reducing the surface tension approximately from 0.04 to 0.02. The comparison between the present simulations (blue snapshots) and experimental results [64] (grey snapshots) at We=249 and 328 is shown in Panel (a) and (b), respectively. Panel (c) gives the numerical predictions of the splashing outcomes at We=540.

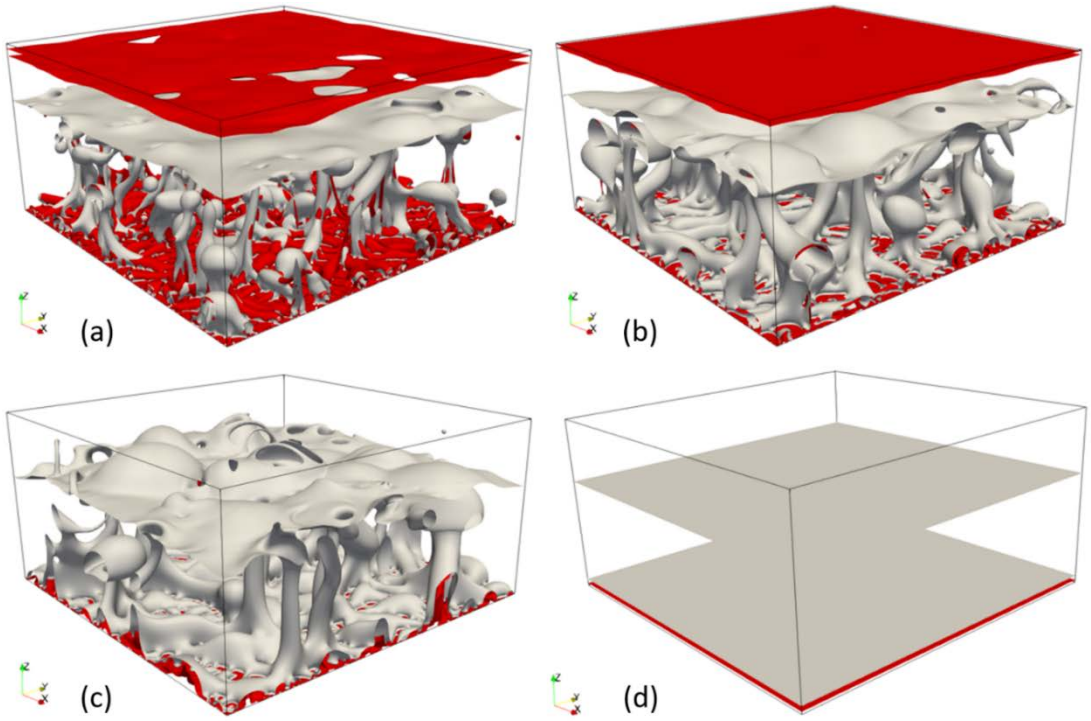

Figure 4: 3D high-resolution simulation of pool boiling by hybrid ULBM (with the CLBM option) finite difference method. The computational domain is a $600\Delta x \times 600\Delta x \times 300\Delta x$ box. In the lattice units, the surface tension is 0.066, the viscosities for the liquid and vapor phases are $\nu_l = 0.1$ and $\nu_g = 0.5/3$, respectively. The characteristic velocity is $u_0 = \sqrt{gl_0} \approx 0.024$ (with gravity $g = 3\times10^{-5}$ and bubble length scale $l_0 \approx 19$), which is much larger than the maximum spurious current $u_s \approx 0.0018$. By varying the wall superheat ΔT, the boiling stages at different Jacob numbers (Ja) can be achieved. The liquid-vapor interface and isothermal surface [$T = 0.5(T_b + T_s)$] are marked by white and red colours, respectively. All the regimes observed in experiments are reproduced: (a) discrete bubble nucleate boiling at $Ja = 0.220$, (b) mushroom bubble nucleate boiling at $Ja = 0.283$, (c) transition boiling $Ja = 0.441$, and (d) film boiling regimes at $Ja = 0.488$ [67].